2026 IEEE RAS/EMBS International Conference on Biomedical Robotics and Biomechatronics (BioRob 2026)
August 1-4, 2026. Edmonton, Canada

Euler-Spiral Kinematic Modeling of a Cable-Driven Continuum Robot with Passive Variable Stiffness for Neurosurgical Applications*

Mojtaba Esfandiari[1†], Fahad Iqbal[2], Hamidreza Hoshyarmanesh[3], Sanju Lama[4], Iulian Iordachita[1], Mahdi Tavakoli[5], and Garnette Sutherland[4]

***Abstract*— This paper presents a variable-curvature kinematic modeling framework for a cable-driven continuum robot with passive, non-uniform structural stiffness along its arc length. The proposed continuum section uses a graded notch pattern, with larger notch spacing near the base and smaller notch spacing toward the distal tip, producing higher proximal stiffness and greater distal flexibility. Conventional constant-curvature models approximate the backbone as a circular arc and may be insufficient for continuum robots whose stiffness varies along their length. To address this limitation, we formulate a mechanically motivated Euler-spiral approximation in which curvature increases along the arc length. The model explicitly uses differential actuation of two antagonistic cable pairs controlling pitch and yaw bending angles. Forward and inverse kinematic relations are derived for the variable-curvature backbone geometry. The proposed model is presented as a simulation-based and mechanically motivated approximation. The framework provides a tractable basis for future experimental identification and model-based control of graded-stiffness continuum robots.**

I. Introduction

Brain tumors pose a significant challenge to patient quality of life, and maximum safe resection remains a primary goal of surgical treatment. To achieve this goal, surgeons must plan access paths that minimize injury to normal brain tissue. However, as minimally invasive surgical approaches become more widely adopted, surgical corridors become narrower, which increases the importance of overcoming line-of-sight limitations.

Surgical instrumentation commonly relies on rigid tools, which can restrict workspace and maneuverability, particularly along narrow or curved surgical pathways. To improve resection control and image-guided precision microsurgery, intra-operative MRI and robotic systems have previously been investigated [1]. Despite these advances, there remains

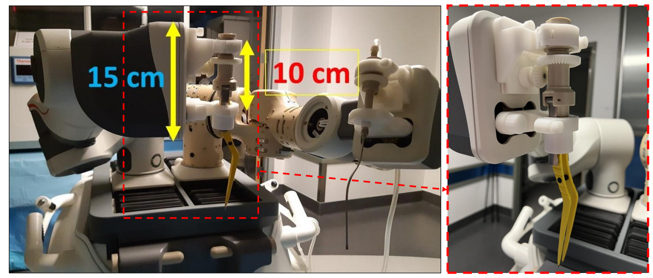

Fig. 1. The SYMBIS robot manipulator (left) and its end-effector mechanism (right): a stereotactic brain biopsy robotic system and second-generation neuroArm system. Dimensional constraints of the actuation unit are shown.

a need for bendable tools that can enable microsurgical manipulation beyond a direct line of sight. Snake-like and continuum robotic technologies offer promising solutions to this challenge, with applications ranging from bariatric surgery [2], to natural orifice transluminal endoscopic surgery [3], to retinal surgery [4], [5], to neurosurgery [6], among others [7], [8], [9].

The long-term goal of this project is to develop a multipurpose continuum robot that can deliver surgical instruments, such as a camera, suction tube, or laser, into regions that are difficult to access using rigid tools. A conceptual CAD model of a single-segment, cable-driven continuum robot with four degrees of freedom (DoF) is shown in Fig. 2. The robot is intended to be mounted onto a robotic microsurgical platform, such as the neuroArm or the SYMBIS robotic systems [10], while satisfying dimensional and workspace constraints.

Inspired by prior cable-driven surgical continuum robots [11], we consider a monolithic tube structure actuated by four cables. In contrast to conventional uniform-stiffness designs, the proposed continuum section uses a graded notch pattern along its length. The notches are spaced farther apart near the base and more closely near the tip. This design creates a passive stiffness gradient: the proximal section remains relatively stiff, while the distal section becomes more compliant. As a result, under cable actuation, the robot is expected to bend preferentially near the tip. This behavior may reduce the swept area of the continuum body for a given tip angle, which is desirable in confined surgical environments.

Kinematic modeling of continuum robots is essential for shape estimation [12], [13], [14] and control [15], [16]. Many existing approaches use constant-curvature models, where

*This work is supported by the Canadian Institutes of Health Research.

[1]Mojtaba Esfandiari and Iulian Iordachita are with the Laboratory for Computational Sensing and Robotics, Johns Hopkins University, Baltimore, MD 21218 USA. (mesfand2; iordachita@jhu.edu)

[2]Fahad Iqbal is with the Department of the Bachelor of Health Sciences, University of Calgary, 2500 University Drive NW, Calgary, Alberta T2N 1N4, Canada. (fahad.iqbal@ucalgary.ca)

[3]Hamidreza Hoshyarmanesh is with the Questrom School of Business, Boston University, Boston, MA 02215, USA.

[4]Sanju Lama and Garnette Sutherland are with the Department of Clinical Neurosciences, University of Calgary, 2500 University Drive NW, Calgary, Alberta T2N 1N4, Canada. (slama; garnette@ucalgary.ca)

[5]Mahdi Tavakoli is with the Department of Electrical and Computer Engineering, University of Alberta, Alberta T6G 1H9, Canada. (mahdi.tavakoli@ualberta.ca)

[†]Corresponding author

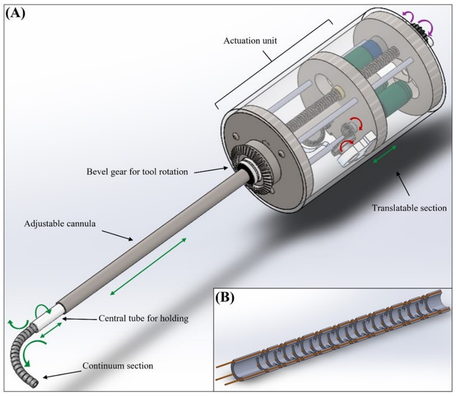

Fig. 2. CAD model of the proposed continuum robot. (A) The 4 DoF are highlighted in green. The central tube allows for insertion and rotation. Internal bevel gear movement is indicated with red arrows. These gears are attached to the motors, and their concomitant movement allows bending of the continuum robot. The two spur gears allow translation of the central tube and continuum section. (B) Cross-section of the continuum section showing three of the four wires. Control of these wires allows bending in two orthogonal planes.

the backbone is approximated as a circular arc. Constant-curvature models are computationally efficient and widely used, but they may be insufficient for continuum robots with non-uniform structural properties. Variable-curvature approaches have therefore been proposed to better represent continuum robot shape, including absolute nodal coordinate formulations and Euler-curve-based representations [15], [17].

In this paper, we propose a variable-curvature kinematic model for a cable-driven continuum robot with graded structural stiffness. The model is based on an Euler-spiral approximation, where curvature varies along the arc length instead of remaining constant. Importantly, the Euler-spiral formulation is used here as a mechanically motivated approximation of the expected curvature distribution caused by non-uniform bending stiffness. Since no physical validation is included in the present work, claims regarding improved accuracy are avoided. Instead, the model is presented as a tractable simulation-based framework for representing distal-compliance-dominant bending. The contributions of this paper are as follows:

- We formulate a variable-curvature kinematic model based on an Euler-spiral approximation for a cable-driven continuum robot with non-uniform stiffness induced by graded notch spacing. We derive forward kinematics for the variable-curvature backbone and express the backbone shape using Fresnel-integral relations.
- We derive inverse kinematic relations using differential actuation of two antagonistic cable pairs that control the pitch and yaw motions of the distal end.

This work presents a simulation-based framework fo the proposed Euler-spiral model. Experimental validation, parameter identification, and control need further evaluation in future work.

The paper is organized as follows. The materials, methods, and design are summarized in Section II. The forward and inverse kinematic modeling framework is presented in Section III. Simulation results are presented in Section IV. Section V concludes the paper and discusses future work.

II. Materials and Methods

The prototype continuum robot is intended to be mounted onto the SYMBIS system. The tool must satisfy the weight and size constraints of the robotic gripper. It is designed as a 4-DoF robot, providing one translational DoF for insertion, one rotational DoF for axial roll, and two bending DoF for the continuum section (Fig. 2). The actuation mechanism is intended to be housed near the SYMBIS end-effector without negatively affecting the workspace, while preserving a central channel for tool delivery.

Given the limited workspace available in many glioma resections, we selected a compact form factor with a central channel that can accommodate small flexible tools such as a laser, camera, or forceps. The continuum section is controlled by four stainless steel wires arranged as two antagonistic cable pairs. The pair (q_{x1}, q_{x2}) controls pitch bending, while the pair (q_{y1}, q_{y2}) controls yaw bending.

The key design feature is the graded notch pattern along the continuum section. Larger notch spacing near the base increases proximal stiffness, whereas smaller notch spacing near the tip increases distal compliance. This non-uniform structural stiffness is expected to produce a variable-curvature shape under tendon actuation, motivating the Euler-spiral kinematic model developed in the following section.

III. Mathematics

A. Forward Kinematic Modeling

This section presents the forward kinematic model of the proposed graded-stiffness continuum robot. Unlike conventional constant-curvature models, which approximate the backbone as a circular arc, the proposed model allows the curvature to vary continuously along the arc length.

Let $s \in [0,l]$ denote the arc-length coordinate measured from the base of the continuum section, where l is the total length of the bendable section. The local curvature is denoted by $\kappa(s)$, the bending angle by $\psi(s)$ (Fig. 3), and the bending-plane angle by φ (Fig. 4).

1) Modeling assumptions: The following assumptions are used:

Assumption 1: The backbone is inextensible and unshearable. Axial stretch and shear deformation are neglected.

Assumption 2: Torsional deformation is neglected. The robot bends in a plane defined by the bending-plane angle φ.

Assumption 3: The effective bending rigidity of the backbone varies along the arc length due to the non-uniform notch spacing. This spatially varying rigidity is denoted by $EI(s)$.

Assumption 4: The curvature increases monotonically from the base toward the tip because the distal section is more compliant than the proximal section.

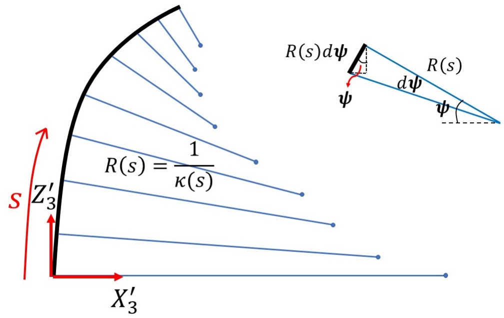

Fig. 3. The variable curvature Euler spiral model sketch. The dependency of the curvature κ on the arc parameter s is shown.

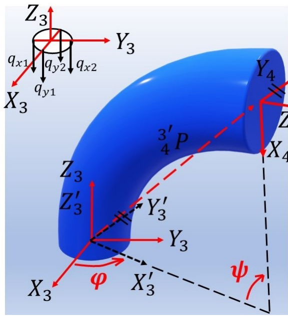

Fig. 4. Schematic 3D shape of the continuum structure and the four actuation cables $q_{x,y,i}$, $i \in \{1,2\}$.

Assumption 5: For tractable kinematic modeling, the curvature profile is approximated by a first-order Euler spiral:

$$\kappa(s) = \alpha(q)\frac{s}{l}, \tag{1}$$

where $\alpha(q)$ is an actuation-dependent curvature gain. This approximation captures the expected increase of curvature along the arc length while retaining a closed-form geometric representation.

The physical motivation for Eq. (1) follows from the Euler-Bernoulli moment-curvature relation:

$$M(s) = EI(s)\kappa(s), \tag{2}$$

where $M(s)$ is the tendon-induced bending moment. Since the graded notch pattern makes the distal section more compliant, $EI(s)$ decreases toward the tip. Therefore, for comparable tendon-induced bending moment, the local curvature increases where $EI(s)$ is lower. The Euler-spiral model in Eq. (1) is therefore used as a low-order approximation of this continuously increasing curvature profile.

A simple linear stiffness-gradient model can be written as

$$EI(s) = EI_0\left(1 - \beta\frac{s}{l}\right), \quad 0 \le \beta < 1, \tag{3}$$

where EI_0 is the proximal bending rigidity and β is a stiffness-gradient parameter. For an approximately constant bending moment M, Eq. (2) gives

$$\kappa(s) = \frac{M}{EI_0\left(1 - \beta\frac{s}{l}\right)}. \tag{4}$$

For small β,

$$\kappa(s) \approx \frac{M}{EI_0}\left(1 + \beta\frac{s}{l}\right). \tag{5}$$

This relation motivates the use of a curvature profile that increases approximately linearly with arc length. In the present work, the constant-curvature offset term is neglected to emphasize distal-compliance-dominant bending, resulting in the Euler-spiral approximation in Eq. (1).

2) Bending angle: The differential change in backbone orientation is

$$d\psi = \kappa(s)ds. \tag{6}$$

Substituting Eq. (1) gives

$$\psi(s) = \int_0^s \alpha(q)\frac{\sigma}{l}d\sigma = \frac{\alpha(q)}{2l}s^2. \tag{7}$$

At the robot tip, $s = l$, the total bending angle is

$$\psi_l = \psi(l) = \frac{\alpha(q)l}{2}. \tag{8}$$

Therefore,

$$\alpha(q) = \frac{2\psi_l}{l}. \tag{9}$$

3) Backbone position in the bending plane: In the local bending plane, the centerline position is obtained from

$$dX' = \sin(\psi(s))ds, \tag{10}$$

$$dZ' = \cos(\psi(s))ds. \tag{11}$$

Using Eq. (7), the planar backbone coordinates are

$$X'(s) = \int_0^s \sin\left(\frac{\alpha(q)}{2l}\sigma^2\right)d\sigma, \tag{12}$$

$$Z'(s) = \int_0^s \cos\left(\frac{\alpha(q)}{2l}\sigma^2\right)d\sigma. \tag{13}$$

Using the Fresnel sine and cosine integrals, the closed-form expressions are

$$X'(s) = \sqrt{\frac{\pi l}{\alpha(q)}}\,\mathfrak{S}\left(\sqrt{\frac{\alpha(q)}{\pi l}}s\right), \tag{14}$$

$$Z'(s) = \sqrt{\frac{\pi l}{\alpha(q)}}\,\mathfrak{C}\left(\sqrt{\frac{\alpha(q)}{\pi l}}s\right), \tag{15}$$

where $\mathfrak{S}(\cdot)$ and $\mathfrak{C}(\cdot)$ are the Fresnel sine and cosine integrals, respectively.

When $\alpha(q) \to 0$, the robot remains straight and

$$X'(s) = 0, \qquad Z'(s) = s. \tag{16}$$

4) Taylor-series approximation: For small bending angles, Eqs. (12) and (13) can be approximated using Taylor expansions:

$$\sin\left(\frac{\alpha}{2l}s^2\right) = \frac{\alpha}{2l}s^2 - \frac{1}{3!}\left(\frac{\alpha}{2l}s^2\right)^3 + \frac{1}{5!}\left(\frac{\alpha}{2l}s^2\right)^5 + \cdots, \tag{17}$$

$$\cos\left(\frac{\alpha}{2l}s^2\right) = 1 - \frac{1}{2!}\left(\frac{\alpha}{2l}s^2\right)^2 + \frac{1}{4!}\left(\frac{\alpha}{2l}s^2\right)^4 + \cdots. \tag{18}$$

After integration,

$$X'(s) = \frac{\alpha}{6l}s^3 - \frac{1}{42}\left(\frac{\alpha}{2l}\right)^3 s^7 + \frac{1}{1320}\left(\frac{\alpha}{2l}\right)^5 s^{11} + \cdots, \quad (19)$$

$$Z'(s) = s - \frac{1}{10}\left(\frac{\alpha}{2l}\right)^2 s^5 + \frac{1}{216}\left(\frac{\alpha}{2l}\right)^4 s^9 + \cdots. \quad (20)$$

5) Cable-displacement mapping: The continuum robot is actuated by four cables arranged as two antagonistic pairs (Fig. 4). The pair (q_{x1}, q_{x2}) controls pitch bending, while the pair (q_{y1}, q_{y2}) controls yaw bending.

The differential cable displacements are defined as

$$\Delta q_x = q_{x2} - q_{x1}, \quad (21)$$

$$\Delta q_y = q_{y2} - q_{y1}. \quad (22)$$

The total effective tendon actuation magnitude is

$$\Delta q = \sqrt{\Delta q_x^2 + \Delta q_y^2}. \quad (23)$$

The bending-plane angle is

$$\varphi = \operatorname{atan2}(\Delta q_y, \Delta q_x). \quad (24)$$

The actuation-dependent curvature gain is modeled as

$$\alpha(q) = k_q \Delta q, \quad (25)$$

where k_q is an actuation-to-curvature coefficient. In this simulation-based study, k_q is treated as a model parameter. In future work, k_q should be experimentally identified from measured backbone shapes.

Combining Eqs. (8) and (25), the total tip bending angle becomes

$$\psi_l = \frac{k_q l}{2}\sqrt{\Delta q_x^2 + \Delta q_y^2}. \quad (26)$$

6) Three-dimensional backbone position: The planar Euler-spiral curve is rotated about the base frame according to the bending-plane angle φ. The three-dimensional backbone coordinates are

$$X(s) = X'(s)\cos\varphi, \quad (27)$$

$$Y(s) = X'(s)\sin\varphi, \quad (28)$$

$$Z(s) = Z'(s). \quad (29)$$

The homogeneous transformation from the base frame to the backbone frame at arc length s can be written as

$$T(s) = R_z(\varphi)R_y(\psi(s))R_z(-\varphi)\begin{bmatrix} I_{3\times 3} & p(s) \\ 0_{1\times 3} & 1 \end{bmatrix}, \quad (30)$$

where

$$p(s) = \begin{bmatrix} X(s) \\ Y(s) \\ Z(s) \end{bmatrix}. \quad (31)$$

Equivalently, the position is obtained from Eqs. (27)–(29), and the local orientation is defined by the accumulated bending angle $\psi(s)$ in the plane φ.

B. Inverse Kinematic Modeling

The inverse kinematic problem is defined as finding cable commands that produce a desired bending-plane angle φ_d and desired tip bending angle ψ_d.

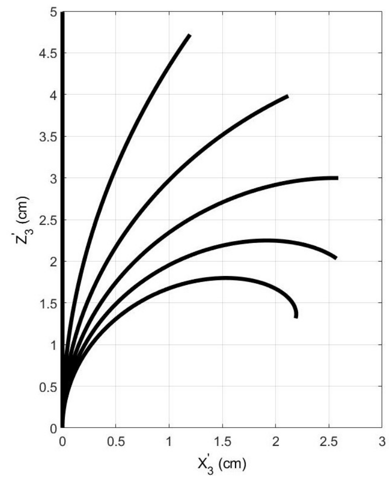

Fig. 5. Shape of the robot centerline in the $X_3'Z_3'$ plane, based on the Euler spirals model at different cable activation levels.

From Eq. (8), the desired curvature gain is

$$\alpha_d = \frac{2\psi_d}{l}. \quad (32)$$

Using Eq. (25), the required differential tendon displacement magnitude is

$$\Delta q_d = \frac{\alpha_d}{k_q} = \frac{2\psi_d}{k_q l}. \quad (33)$$

The desired pitch and yaw differential displacements are then

$$\Delta q_x = \Delta q_d \cos\varphi_d, \quad (34)$$

$$\Delta q_y = \Delta q_d \sin\varphi_d. \quad (35)$$

Because the cables can pull but cannot push, one feasible cable-command is

$$q_{x1} = \max(0, -\Delta q_x), \qquad q_{x2} = \max(0, \Delta q_x), \quad (36)$$

$$q_{y1} = \max(0, -\Delta q_y), \qquad q_{y2} = \max(0, \Delta q_y). \quad (37)$$

This relation applies when cable commands are represented as pull-only displacements from a zero reference.

C. Relation to the Constant-Curvature Model

The conventional constant-curvature model assumes

$$\kappa(s) = \kappa_0, \quad (38)$$

which gives

$$\psi(s) = \kappa_0 s. \quad (39)$$

The corresponding planar backbone position is

$$X_{cc}(s) = \frac{1 - \cos(\kappa_0 s)}{\kappa_0}, \quad (40)$$

$$Z_{cc}(s) = \frac{\sin(\kappa_0 s)}{\kappa_0}. \quad (41)$$

In contrast, the proposed Euler-spiral model uses

$$\kappa(s) = \alpha(q)\frac{s}{l}, \quad (42)$$

so that curvature increases along the arc length. This distinction is important for graded-stiffness continuum robots,

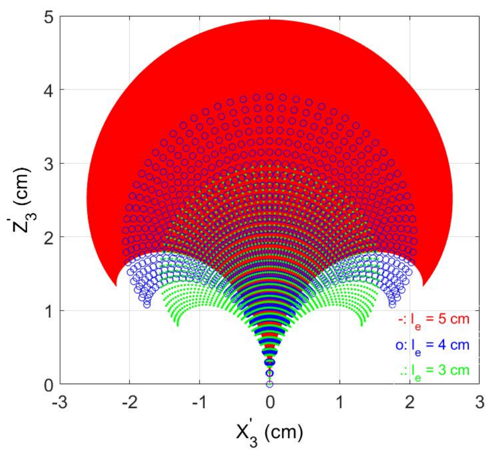

Fig. 6. Area swept by the continuum robot in the $X_3^{'}Z_3^{'}$ plane, at three exposed lengths of the continuum section $l_e = 3,4,5$ cm.

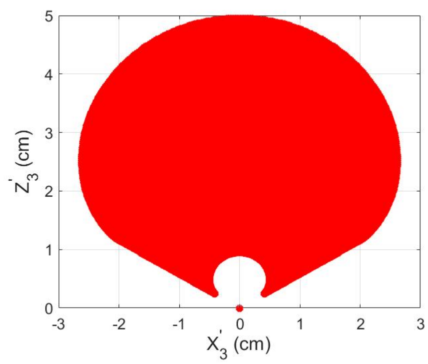

Fig. 7. Continuum robot's reachable workspace, footprint of the continuum section tip on the $X_3^{'}Z_3^{'}$ plane for $1cm \leq l_e \leq 5cm$ and cable displacements $0 \leq q_{x,y,i} \leq 10mm$, $i \in \{1,2\}$.

where the distal portion is more compliant than the proximal portion. The constant-curvature model is therefore used only as a reference model, while the proposed variable-curvature model is intended to approximate the effect of spatially varying stiffness.

D. Limitations of the Model

The proposed model is based on several simplifying assumptions. First, the backbone is assumed to be inextensible and unshearable. Second, torsion is neglected. Therefore, configurations involving substantial twist, compression, or out-of-plane deformation are outside the scope of the present formulation. Third, the Euler-spiral curvature profile is used as a first-order approximation of the expected variable-curvature behavior caused by graded stiffness. Finally, since this work does not include experimental validation, the model should be interpreted as a simulation-based kinematic approximation. Experimental shape tracking and parameter identification are required to evaluate model accuracy in future work.

IV. Simulation Results

By solving the forward kinematics, robot's configuration is calculated for various cable displacements (Fig. 5). The area swept by the continuum robot body in the $X_3^{'}Z_3^{'}$ plane is shown for three exposed lengths of the continuum section $l_e = 3,4,5$ cm (Fig. 6). Robot's reachable workspace, continuum section tip footprint, is determined for $1 \leq l_e \leq 5$ cm and $0 \leq q_{x,y,i} \leq 10$ mm (Fig. 7).

Also, the kinematic performance analysis of the robot is studied using the condition number (ζ), as a measure of the columns' independence in the robot's Jacobian matrix [18]. The condition number of a full-rank Jacobian matrix is $\zeta = \frac{\sigma_{max}}{\sigma_{min}}$, where σ_{max}, σ_{min} are the maximum and minimum singular values of the Jacobian. A manipulator configuration in which the condition number is close to unity is called an isotropic configuration. This means that the manipulator is well conditioned and the Jacobian matrix singular values are close to each other. Given that the calculation of the condition number with this relation is not simple and since our Jacobian matrix ($J_{6\times5}$) is not a square matrix, we used another relation to calculate the condition number that is more computationally efficient as,

$$\zeta = ||J||||J^{\dagger}|| \tag{43}$$

where $||J||$ is the norm and $J^{\dagger}$ is the pseudoinverse of the rectangular matrix $J_{6\times5}$.

A. Local and Global Conditioning Indices

Since the condition number is not upper bounded ($1 < \zeta < \infty$), another method for the local performance measure, the local conditioning index (LCI), is used, which is the inverse of the condition number LCI=$\frac{1}{\zeta}$, and is bounded LCI $\in (0,1)$ and is independent of scale. The closer to the unity the LCI is, the better kinematic performance the robot shows. Figure 8, in which one cable is activated (q) to bend the robot, shows that the robot has an LCI close to 0.7. The global conditioning index (GCI) introduced by [19] represents the general conditioning of the robot over the entire workspace w, and is computed (GCI = 0.708) using the following formula,

$$GCI = \frac{\int_w \frac{1}{\zeta} dw}{\int_w dw} = \frac{\int_\Theta \frac{1}{\zeta} \Delta d\theta_1 d\theta_2 \cdots d\theta_n}{\int_\Theta \Delta d\theta_1 d\theta_2 \cdots d\theta_n} \tag{44}$$
$$\Delta = \sqrt{det(JJ^T)}$$

V. Conclusions

Complex gliomas pose a difficult challenge, as accessing all cancerous masses must be balanced with the amount of healthy tissue that is removed to create clear, straight corridors to the tumour site. Small, flexible tool delivery platforms can help mitigate this limitation by allowing access to several tumours in a region without the removal of large areas of the brain. In this paper, kinematic modeling for a continuum robot is studied using Euler spirals. The continuum robot's workspace in 2D space is determined and the LCI and GCI indices are measured for the kinematic performance

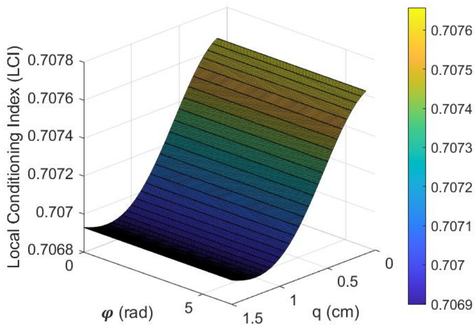

Fig. 8. Local conditioning index LCI level of the robot tip Jacobian versus activation of one cable q for the entire range of φ.

analysis. As opposed to the constant curvature models that consider the curved robot as a section of a circle, curvature of the robot centerline in this model is dependent to the arc length parameter s. In the future experiments, optimization algorithms will be used for both design parameters selection and path planning in the presence of physical constraints.

APPENDIX

The Jacobian matrix that maps the actuator space velocities $\dot{\Theta}$ to the robot's task space velocities is calculated as,

$$[{}^0v_4, {}^0w_4]^T = {}^0J\dot{\Theta} \tag{45}$$

$${}^0J = \begin{bmatrix} -X_3' s(\theta_2+\varphi) & 0 & 0 & -X_3' s(\theta_2+\varphi) & Z_3' c(\theta_2+\varphi) \\ X_3' c(\theta_2+\varphi) & 0 & 0 & X_3' c(\theta_2+\varphi) & Z_3' s(\theta_2+\varphi) \\ 0 & 1 & 1 & 0 & -X_3' \\ 0 & 0 & 0 & 0 & -s(\theta_2+\varphi) \\ 0 & 0 & 0 & 0 & c(\theta_2+\varphi) \\ 1 & 0 & 0 & 1 & 0 \end{bmatrix} \tag{46}$$

Where ${}^0v_4, {}^0w_4$ are the linear and angular velocities, respectively, of the continuum robot tip frame $\{G\}$ relative to the manipulator end-effector frame $\{E\}$ (Fig. 9).

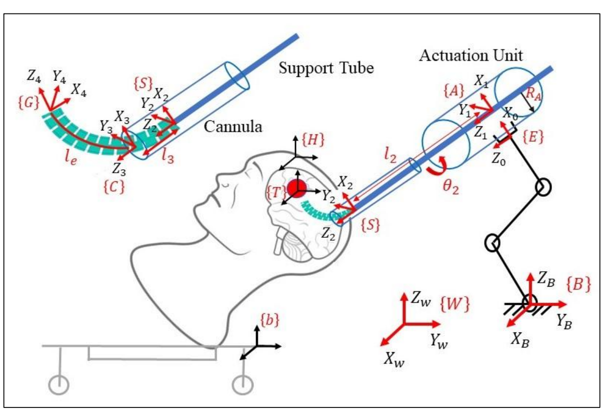

Fig. 9. Schematic of different frames attached to the SYMBIS manipulator, the proposed continuum robot actuation mechanisms, and patient.

REFERENCES

[1] G. R. Sutherland, S. Wolfsberger, S. Lama, and K. Zarei-nia, "The evolution of neuroarm," *Neurosurgery*, vol. 72, no. suppl_1, pp. A27–A32, 2013.

[2] X. Zhang, W. Li, P. W. Y. Chiu, and Z. Li, "A novel flexible robotic endoscope with constrained tendon-driven continuum mechanism," *IEEE Robotics and Automation Letters*, vol. 5, no. 2, pp. 1366–1372, 2020.

[3] P. Qi, C. Zhang, J. Li, Z. Li, J. S. Dai, and K. Althoefer, "A compact continuum manipulator system with enhanced steering abilities for robot-assisted surgery," in *2016 6th IEEE International Conference on Biomedical Robotics and Biomechatronics (BioRob)*. IEEE, 2016, pp. 49–54.

[4] M. Esfandiari, Y. Zhou, S. Dehghani, M. Hadi, A. Munawar, H. Phalen, D. E. Usevitch, P. Gehlbach, and I. Iordachita, "A data-driven model with hysteresis compensation for i 2 ris robot," in *2024 International Symposium on Medical Robotics (ISMR)*. IEEE, 2024, pp. 1–7.

[5] P. Du, M. Esfandiari, H. Wei, M. Jinno, P. Gehlbach, A. Munawar, P. Kazanzides, and I. Iordachita, "Dual-ekf system identification and model predictive path integral control of a retinal microsurgical robot," *Journal of Medical Robotics Research*, 2026.

[6] Y. Kim, S. S. Cheng, M. Diakite, R. P. Gullapalli, J. M. Simard, and J. P. Desai, "Toward the development of a flexible mesoscale mri-compatible neurosurgical continuum robot," *IEEE Transactions on Robotics*, vol. 33, no. 6, pp. 1386–1397, 2017.

[7] H.-S. Yoon, J. H. Jeong, and B.-J. Yi, "Image-guided dual master–slave robotic system for maxillary sinus surgery," *IEEE Transactions on Robotics*, vol. 34, no. 4, pp. 1098–1111, 2018.

[8] T. da Veiga, J. H. Chandler, P. Lloyd, G. Pittiglio, N. J. Wilkinson, A. K. Hoshiar, R. A. Harris, and P. Valdastri, "Challenges of continuum robots in clinical context: a review," *Progress in Biomedical Engineering*, vol. 2, no. 3, p. 032003, 2020.

[9] F. Iqbal, M. Esfandiari, G. Amirkhani, H. Hoshyarmanesh, S. Lama, M. Tavakoli, and G. R. Sutherland, "Continuum and soft robots in minimally invasive surgery: A systematic review," *IEEE Access*, vol. 13, pp. 24 053–24 079, 2025.

[10] M. J. Lang, A. D. Greer, and G. R. Sutherland, "Intra-operative robotics: Neuroarm," in *Intraoperative Imaging*. Springer, 2010, pp. 231–236.

[11] R. J. Murphy, M. D. Kutzer, S. M. Segreti, B. C. Lucas, and M. Armand, "Design and kinematic characterization of a surgical manipulator with a focus on treating osteolysis," *Robotica*, vol. 32, no. 6, pp. 835–850, 2014.

[12] G. Amirkhani, A. Goodridge, M. Esfandiari, H. Phalen, J. H. Ma, I. Iordachita, and M. Armand, "Design and fabrication of a fiber bragg grating shape sensor for shape reconstruction of a continuum manipulator," *IEEE Sensors Journal*, vol. 23, no. 12, pp. 12 915–12 929, 2023.

[13] Y. Yue, M. Esfandiari, P. Du, P. Gehlbach, M. Jinno, A. Munawar, P. Kazanzides, and I. Iordachita, "An extended generalized prandtl-ishlinskii hysteresis model for i2ris robot," *IFAC-PapersOnLine*, vol. 59, no. 30, pp. 323–328, 2025.

[14] S. Zhu, Y. Heo, M. Esfandiari, H. Ishida, L. Seenivasan, P. Kazanzides, P. Gehlbach, I. Iordachita, and A. Munawar, "A high-fidelity synthetic data generation toolkit for vision-based localization models in intraocular robotic microsurgery," *Journal of Medical Robotics Research*, 2026.

[15] X. Huang, J. Zou, and G. Gu, "Kinematic modeling and control of variable curvature soft continuum robots," *IEEE/ASME Transactions on Mechatronics*, vol. 26, no. 6, pp. 3175–3185, 2021.

[16] M. Esfandiari, P. DuM, H. Wei, P. Gehlbach, A. Munawar, P. Kazanzides, and I. Iordachita, "Model predictive path integral control of i 2 ris robot using rbf identifier and extended kalman filter," in *2025 American Control Conference (ACC)*. IEEE, 2025, pp. 3341–3347.

[17] P. S. Gonthina, A. D. Kapadia, I. S. Godage, and I. D. Walker, "Modeling variable curvature parallel continuum robots using euler curves," in *2019 International Conference on Robotics and Automation (ICRA)*. IEEE, 2019, pp. 1679–1685.

[18] S. Patel and T. Sobh, "Manipulator performance measures-a comprehensive literature survey," *Journal of Intelligent & Robotic Systems*, vol. 77, no. 3, pp. 547–570, 2015.

[19] C. Gosselin and J. Angeles, "A global performance index for the kinematic optimization of robotic manipulators," 1991.